ELSEVIER

Contents lists available at ScienceDirect

#### Ceramics International

journal homepage: www.elsevier.com/locate/ceramint





### Phenomenological sintering model and experimental validation of gravity-induced distortions in binder-jetted stainless steel components

Alberto Cabo Rios a,b,\*, Mats Persson , Eduard Hryha , Eugene Olevsky b,d

- <sup>a</sup> Department of Industrial and Materials Science, Chalmers University of Technology, Gothenburg, Sweden
- <sup>b</sup> Mechanical Engineering, San Diego State University, San Diego, USA
- <sup>c</sup> Digital Metal AB, Höganäs, Sweden
- <sup>d</sup> NanoEngineering, University of California, San Diego, La Jolla, USA

#### ARTICLE INFO

Handling Editor: Dr P. Vincenzini

Keywords:
Binder jetting
Additive manufacturing
Sintering
Modelling

#### ABSTRACT

Sintering is an important consolidation step employed in sinter-based metal additive manufacturing processes. Binder Jetting (BJT) starts with green components with low green density (40–60 %) that results in large sintering shrinkages and geometrical shape distortions caused by external forces (e.g. gravity). Consequently, the prediction of the final sintered geometry is crucial during the design process. In this work, a novel sintering simulation framework for gravity-affected sintering of stainless-steel components is presented, including the Rios-Olevsky-Hryha sintering model and the methodology for the identification of the required material parameters. The constitutive law includes material constants to account for the powder packing effects and the delta-ferrite transformation occurring at high temperatures. The material shear viscosity was explicitly related to the equilibrium phase fraction of austenite and delta-ferrite during sintering temperatures. Dilatometry experiments were conducted and followed by the data postprocessing for the model calibration. The calibrated model was incorporated in a FEM code and validated against experimental data from BJT sintered components, showing the remarkably accuracy of the numerical simulations, with small geometric deviations (0.56 mm) related to the assumption of isotropic shrinkage in the model proposed. In parallel, other alternative models were implemented based on different normalized bulk viscosity formulations, which underestimate/overestimate the sintered distortions.

#### 1. Introduction

Metal Binder Jetting Technology (BJT) has become a transformative force in the industrial manufacturing landscape, revolutionizing the production of metallic components. This innovative additive manufacturing (AM) process is being widely adopted across industries as a cost-effective solution for small to medium-sized production runs, reducing material waste and promoting sustainability [1–3]. Overall, Metal Binder Jetting represents a paradigm shift, offering benefits such as intricate design capabilities, cost efficiency, rapid prototyping, and enhanced design flexibility, with the potential to reshape traditional manufacturing practices. One of the key advantages of BJT over other AM techniques is the ability to achieve mass-production levels similar to other powder metallurgy manufacturing methods like metal injection molding (MIM) without extensive development efforts due to the similarities between the consolidation steps in these manufacturing process.

Binder Jetting (BJT) is a multi-step AM process, where two principal steps can be differentiated [4]. The first step is the BJT printing where the geometrical shape is given to the green component in a layer-by-layer process in which a liquid bonding agent is selectively deposited on the top of a powder bed to join powder particles. The second step consists of the processes by which the final properties (i.e. mechanical and other functional properties) of the components are achieved by the consolidation of the metal powder material. Typically, the processes during the second step include the debinding and sintering of the BJT green components. The debinding process involves controlled heating in a specific atmosphere to volatilize and remove the binders to prevent unwanted residues and to ensure the desired material properties in the final sintered part [5,6]. During debinding, the component's geometry does not change notably since the low temperatures used are not sufficient to cause densification of the powder compact [6-8]. Then, the sintering process is a key step where the green component evolves until the final geometry and properties are reached. Because of the inherent

<sup>\*</sup> Corresponding author. Department of Industrial and Materials Science, Chalmers University of Technology, Rännvägen 2A, Gothenburg, 412 96, Sweden. E-mail address: cabo@chalmers.se (A. Cabo Rios).

Nomenclature		t	Time $(s)$
		G	Grain size diameter (m)
ρ	Density	$k_0$	Grain growth pre-exponential factor $(\mu m^3 \bullet s^{-1})$
$\theta$	Porosity	$Q_{ m G}$	Grain growth activation energy $(J \bullet mol^{-1})$
$\dot{ heta}$	Porosity elimination rate $(s^{-1})$	$ ho_c$	Grain growth critical density
$\sigma_{ij}$	Stress tensor $(N \bullet m^{-2})$	A	Powder packing fitting parameter
$\dot{oldsymbol{arepsilon}}_{ij}$	Strain rate tensor $(s^{-1})$	В	Powder packing fitting parameter
ė	Trace of the strain rate tensor $(s^{-1})$	$ heta_c$	Critical porosity fitting parameter
$\delta_{ij}$	Delta de Kronecker	R	Gas constant 8.314 $(J \bullet mol^{-1} \bullet K^{-1})$
$\varphi$	Normalized shear modulus	T	Temperature $(K)$
Ψ	Normalized bulk modulus	$ ho_{\it th}$	Powder material theoretical density $(kg \bullet m^{-3})$
$P_L$	Effective sintering stress (Pa)	$f_{\gamma}$	Austenite phase fraction
α	Surface energy $(J \bullet m^{-2})$	$f_\delta$	Delta ferrite phase fraction
$\eta_0$	Material shear viscosity $(Pa \bullet s)$	$A_{\gamma}$	Austenite's viscosity pre-exponential factor ( $Pa \bullet s \bullet K^{-1}$
$\sigma_{kk}$	Volumetric stress $(N \bullet m^{-2})$	$oldsymbol{A}_{\delta}$	Delta ferrite's viscosity pre-exponential factor
$\sigma_{ij}^{'}$	Deviatoric stress tensor $(N \bullet m^{-2})$		$(Pa \bullet s \bullet K^{-1})$
	Inelastic strain rate tensor $(s^{-1})$	$Q_{\gamma}$	Austenite's viscosity activation energy $(J \bullet mol^{-1})$
$\dot{oldsymbol{arepsilon}}_{ij}^{in}$	,	$Q_{\delta}$	Delta ferrite's viscosity activation energy $(J \bullet mol^{-1})$
$\dot{oldsymbol{arepsilon}}_{ij}^{el}$	Elastic strain rate tensor $(s^{-1})$		, 0, ( )

low relative green density of the BJT components (40–60 %), the components undergo extensive shrinkage (up to  $\sim\!25$  %) during the sintering process, depending on the difference between the green and sintered density [6–11]. Also, the high temperatures required for the sintering of metallic powders may cause geometrical shape distortions during sintering that are retained in the sintered components. Therefore, a thorough understanding of the component's behavior during the sintering process is crucial for the successful industrial implementation of metal binder jetting technologies (BJT).

Achieving the desired final sintered geometry involves designing pre-compensated CAD geometries for the BJT printing step [12-14]. Utilizing scaling factors derived from experimental data may be reliable for offsetting the sintering volumetric shrinkages. However, compensating for shape distortions caused by gravitational and frictional forces is more challenging, as these distortions are intricately linked to the complexity of the initial component geometry. A typical industrial approach to tackle this issue is employing live setters during sintering: supporting structures that are printed and sintered alongside the components but discarded afterward. But this method heavily relies on trial-and-error runs and the operator's engineering skills to design effective support structures. The use of simulation tools is one of the most promising approaches, allowing for the prediction of volumetric shrinkages and geometrical shape distortions of the BJT components during sintering. This opens the possibility for accurate pre-compensation of the sintering distortions directly on the CAD geometry [15]. Also, other microstructural details like relative density and grain size can be predicted by these models.

Sintering simulations using continuum mechanics models, which can be implemented using finite element methods (FEM), have been studied for several decades [16–33]. Initially, the modelling efforts were focused on the understanding of the underlying physics of the sintering phenomena, focusing on cluster of particles at the meso-scale [33]. Subsequently, the main interest was shifted to the macroscale modeling of the sintering process, where real complex geometries can be simulated [17, 22–25,34]. In this context, the continuum theory of sintering was developed by Olevsky [17]. Typically, BJT components are subjected to pressure-less sintering, and the green compacts have some particularities that arise the necessity for further development of the existent models. Particularly, BJT components have an inherently low green density which expands the porosity ranges where the initial and intermediate stage of sintering occurs. In a prior study [11], these sintering stages were explored by limiting temperatures below delta-ferrite

transformation, proposing and validating a new modelling framework. Still, expansion to the entire sintering process of stainless-steel BJT components, typically sintered at high temperatures (>1300 °C) with delta-ferrite phase formation, demands additional development. Previous studies uncovered the delta-ferrite's impact on the microstructure of stainless-steel and the boosted sintering behavior [7,8,35-38]. Certain models have managed to predict the enhanced densification kinetics by dividing the sintering model into steps based on porosity range [39,40], or dividing the sintering on several temperature regions [41]. However, these models do not delve into the specific details of the underlying physical phenomena. Hence, it may be relevant to explicitly consider the delta-ferrite transformation effect within the sintering parameters. A previous study [35] shows an initial effort to include the effect of delta-ferrite phase transformation on the sintering densification kinetics of 316L stainless steel BJT. The study revealed the temperature dependency of this effect, suggesting the time variable influence of the phase transformation is negligible for moderate heating rates compared to the temperature variable's impact. The phase transformation effect was integrated into material shear viscosity  $\eta_0$ , which is theoretically affected by any solid phase microstructure changes and independent of porosity. Yet, implementing and validating such models in a boundary-value continuum mechanics problem is pending. In BJT manufacturing, the prediction of complex geometry' evolution during sintering under external forces (e.g., gravity) at the continuum scale remains a challenge.

In the present paper, a new framework for the sintering simulation of stainless-steel components manufactured by binder jetting (BJT) was introduced. The framework includes the phenomenological model of sintering and the corresponding material's constant identification methodology. The Rios-Olevsky-Hryha (ROH) phenomenological sintering model was developed based on the continuum theory of sintering [17] and subsequent studies [11,35], including the effect of typical low green density of BJT components and the dual phase microstructure (i.e. austenite and delta-ferrite) of stainless-steel during the typically high sintering temperatures (>1300  $^{\circ}$ C). Also, two alternative models were studied by implementing alternative normalized bulk viscosities expressions inspired in a previous study [11]. Then, a methodology for the material constants identification was proposed, based on non-linear fitting methods together with the pre-processing of dilatometry (density) and microstructural data (grain size). Following the material properties identification, the different models were implemented in FEA software. A first set of "tree" geometries were sintered and used for the

validation of the shrinkage, shape deformation and densification predicted by the simulations. A second set of angled beams geometries was used to address the influence of boundary conditions (i.e. contact or rolling boundaries) during the simulation of sintering of BJT components.

#### 2. Experiments and methods

#### 2.1. Materials and BJT system

The gas atomized powder DM 316L and Binder Jetting printer DM P2500 from Digital Metal were used for the manufacturing of the green components. The powder size distribution is defined by the values of 8  $\mu m$  (D $_{10}$ ), 16  $\mu m$  (D $_{50}$ ) and 26  $\mu m$  (D $_{90}$ ), and the chemical composition of the powder is depicted in Table 1. The Digital Metal commercially developed printing parameters were employed, where a layer thickness of 42  $\mu m$  was set. After printing, curing and depowdering, the parts were debinded in air at 345 °C for 2h.

#### 2.2. Design and sintering of tree-shape and angled beam components

Different components have been designed to evaluate the effect of gravity on the distortions of overhang structures during the sintering step. Two "tree geometries" were designed with three branches of straight overhangs with a thickness of 3 mm (Fig. 1(a)) and 2 mm (Fig. 1 (b)) and lengths of 20, 15 and 10 mm (from bottom to top). Also, a second group of 4 geometries were designed with overhangs at different angles and lengths. The green components with overhang beams at 75°,  $45^{\circ}$ ,  $15^{\circ}$  with lengths of 13 mm and 10 mm are shown in Fig. 1(c) and (d), respectively. The green components with overhang beams at 90°,  $60^{\circ}$ ,  $30^{\circ}$  with lengths of 12 mm and 10 mm are shown in Fig. 1(e) and (f), respectively.

After the debinding, the components were transported to and sintered in an industrial batch furnace using hydrogen atmosphere. The sintering was done at 3  $^{\circ}$ C/min heating rate up to 1370  $^{\circ}$ C with a dwell time of 3 h followed by final furnace cooling down to room temperature.

#### 2.3. Dilatometry experiments

Cubical samples with dimensions  $10\times10\times10~\text{mm}^3$  were manufactured along with the components. Then, after debinding the cubical samples were pre-sintered at 900 °C for 60 min following the same process and equipment described in the previous section 2.2. With the purpose of collecting the required experimental data, the cubical samples were sintered using Netzsch DIL 402C dilatometer system. Different samples were sintered following the heating rates and dwell times detailed in Table 2, followed by cooling at a rate of 30 °C/min. All the samples were oriented in the dilatometer with the pushrod parallel to the Z axis (building direction) of the sample [8]. The dilatometry sintering treatments were done under hydrogen atmosphere (purity 6.0), seeking to reproduce the atmosphere used in the industrial batch furnace.

#### 2.4. Density, microstructure and geometry characterization

The green and sintered density of the cubical samples was calculated from the cube's weight and dimensions measurements (geometry-based density) following the same procedure used in previous studies [7,8]. However, for the BJT components (trees and angled beams), the green density was estimated by using the calculated volume from the CAD file

(due to the complex geometry) and the measured green sample weight (geometry-based density). Finally, the sintered density for all components and cubical samples was measured following the Archimedes method.

Microstructural analysis of the sintered samples was done by traditional metallurgical preparation of the samples (cross-sectioning, mounting, grinding, and polishing), followed by the inspection using an automated Zeiss Axioscope 7 light optical microscope (LOM) system. Separately, Electron Backscattered Diffraction (EBSD) was done using a Zeiss Leo Gemini 1550 (FEG-SEM) equipped with a Symmetry detector (Oxford Instruments) and the AZtecCrystal software to post-process the crystallographic information of the microstructure. For the acquisition of EBSD maps an acceleration voltage of 20 KeV and a step size of 0.5  $\mu m$  was used. Finally, the sintered geometry of the BJT "tree" components was characterized using X-ray computed tomography (CT) with a Nikon XT series (Nikon Metrology Ltd, UK).

#### 3. Simulation framework

#### 3.1. Continuum model for free sintering of BJT stainless-steel parts

The sintering process of BJT components can be simulated at the macro-scale by using continuum mechanics sintering models, which can be solved through its implementation on FEA software tools. In addition to predicting geometric changes, these models can also predict the evolution of microstructural details, such as relative density and grain size. The proposed phenomenological ROH (Rios-Olevsky-Hryha) sintering model, based on the theory of sintering [17], has been developed for the prediction of sintering of BJT stainless-steel components. The linear-viscous behavior of the BJT components during the pressure-less sintering process is described by the following constitutive equation:

$$\boldsymbol{\sigma}_{ij} = 2\eta_0 \left[ \varphi \dot{\boldsymbol{e}}^*_{ij} + \left( \psi - \frac{1}{3} \varphi \right) \dot{e} \delta_{ij} \right] + P_L \delta_{ij}$$
 (1)

However, the inverse relationship of this equation can be described as a function of the volumetric  $(\sigma_{kk})$  and deviatoric  $(\sigma_{ij})$  stress components, where now the inelastic contribution to the strain rates can be calculated as follows:

$$\dot{\boldsymbol{\varepsilon}}_{ij}^{in} = \frac{\boldsymbol{\sigma}_{ij}'}{2\eta_0 \varphi} + \frac{\sigma_{kk} - P_L}{18\eta_0 \psi} \delta_{ij} \tag{2}$$

where  $\eta_0$  is the shear viscosity of the porous body's skeleton material (i. e. shear viscosity of the fully dense body),  $P_L$  is the effective sintering stress and  $\delta_{ij}$  is the Kronecker delta function.  $\varphi$  and  $\psi$  are functions of porosity that characterize the normalized shear and bulk moduli of the porous compact.  $\dot{e}$  is the first invariant of the strain rate tensor, which corresponds to the volumetric shrinkage rate. The total strain rate in the sintering component is described by the combination of inelastic and elastic strains [42], where the elastic response of the material is assumed to be isotropic and described by the Hooke's Law.

$$\dot{\boldsymbol{\varepsilon}}_{ii}^{total} = \dot{\boldsymbol{\varepsilon}}_{ii}^{el} + \dot{\boldsymbol{\varepsilon}}_{ii}^{in} \tag{3}$$

The resistance to densification of BJT components was analyzed and studied in detail in a previous work [11], where the potential influence of the powder packing characteristics on the bulk viscosity was comprised in a modified normalized bulk viscosity expression  $\psi$  which contains two different "powder packing constants" (A, B):

Table 1
Chemistry of the DM 316L powder (wt.%).

Cr	Ni	Mo	Mn	Si	С	P	S	0	N	Fe
17.1	11.5	2.2	1.30	0.70	0.024	-	0.006	0.049	0.090	Bal.

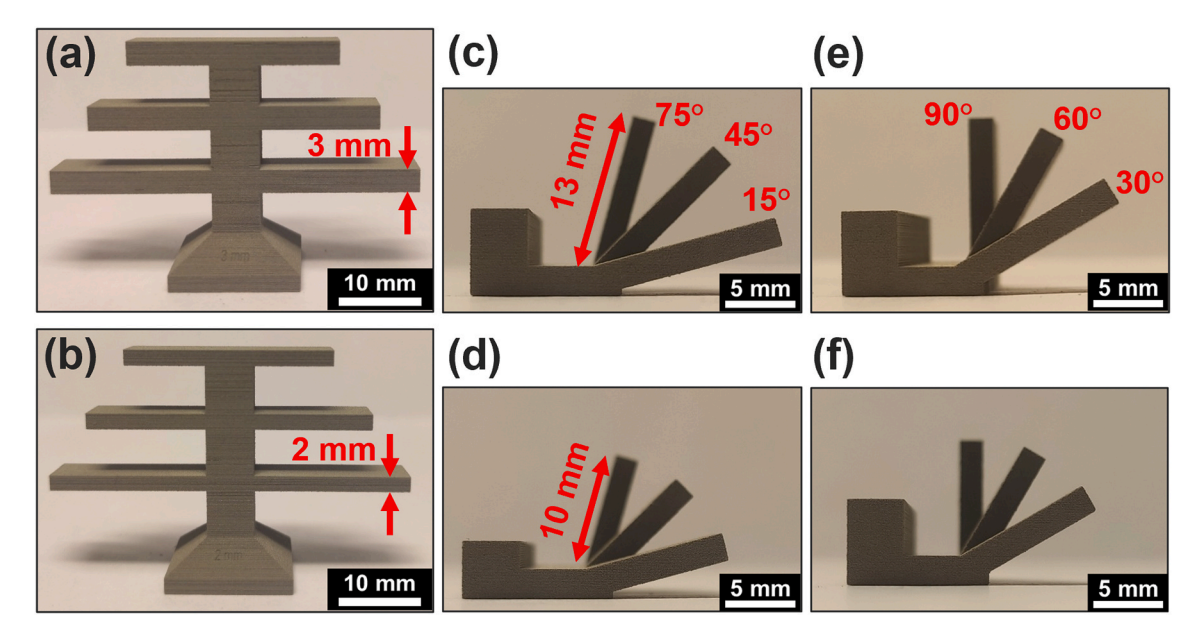


Fig. 1. BJT printed components with overhangs: (a–b) tree components with different overhangs thickness and (c–f) components with overhangs at different angles and lengths.

 Table 2

 Sintering dilatometry treatments for the BJT cubes.

	•		
Sample ID	Heating rate (°C/ min)	Dwell Temperature (°C)	Dwell Time (min)
HR2-1370-60 HR5-1370-60 HR5-1370- 150 HR15-1370- 60	2 5	1370	60 60 150

$$\psi = \frac{2}{3} \frac{(1-\theta)^A}{\theta^B} \tag{4}$$

These constants were suggested to be linked to the morphology of the porous structure, thus determined by the arrangement and size distribution of powder particles in the green components. Besides, the normalized shear viscosity derived by Skorohod [43] was used:

$$\varphi = (1 - \theta)^2 \tag{5}$$

As described in the previous work [11], the following expression for the effective sintering stress, which includes the grain size evolution, is used in the model:

$$P_L = 3\alpha \frac{\left(1 - \theta\right)^2}{G/2} \tag{6}$$

where  $\alpha$  is the specific surface energy and G is the grain diameter.

The kinetic equation proposed by Olevsky et al. [44] was used for the prediction of the grain size evolution during sintering:

$$\frac{dG}{dt} = \frac{k_0}{3G^2} \left(\frac{1 - \rho_c}{2 - \rho_c - \rho}\right)^{3/2} exp\left(\frac{-Q_G}{RT}\right)$$
 (7)

where  $k_0$  is the grain growth pre-exponential term, Q is the activation energy, and  $\rho_c$  is the critical density parameter.

The porosity evolution during sintering is driven by the mass conservation law, which is described as a function of the inelastic volumetric shrinkage rate as follows:

$$\frac{\dot{\theta}}{(1-\theta)} = \dot{\varepsilon}_x^{in} + \dot{\varepsilon}_y^{in} + \dot{\varepsilon}_z^{in} = \dot{e} \tag{8}$$

## 3.2. Stainless steel material shear viscosity $(\eta_0)$ : from austenitic $(\gamma)$ to dual phase $(\gamma + \delta)$ microstructure

The temperature-dependent shear viscosity of the powder solid material  $\eta_0$  is typically described by the Arrhenius function [45]. However, during the sintering of stainless steels, the microstructure transforms from fully austenitic (FCC) to a dual-phase microstructure with the formation of the  $\delta$ -ferrite (BCC) phase at high temperatures [7,8]. This causes a change in the sintering behaviour by increasing the internal diffusion rate and, consequently, the macroscopic shrinkage rate of the parts. This change on the solid material microstructure should be reflected on the temperature-dependent evolution of powder shear viscosity  $\eta_0$ . Previously, a piece-wise Arrhenius function proposed in Ref. [35] was used to predict the densification affected by the delta-ferrite phase. However, one of the drawbacks is the absence of explicit consideration of the phase fractions on the evolution of the material viscosity, which limits its application to the specific stainless-steel composition studied. In the present paper, a more comprehensive equation is proposed inspired on the concept of "rule of mixtures" and the Reuss model [46,47]:

$$\eta_0 = \frac{1}{\frac{f_{\gamma}}{\eta_{\gamma}} + \frac{f_{\delta}}{\eta_{\delta}}} = \frac{1}{f_{\gamma} / A_{\gamma} T \exp\left(\frac{Q_{\gamma}}{RT}\right) + f_{\delta} / A_{\delta} T \exp\left(\frac{Q_{\delta}}{RT}\right)}$$
(9)

where  $A_{\gamma},A_{\delta}$  are the pre-exponential terms and  $Q_{\gamma},Q_{\delta}$  the activation energies constants of the Arrhenius viscosity for the Austenite ( $\gamma$ ) and  $\delta$ -ferrite ( $\delta$ ).  $f_{\gamma},f_{\delta}$  are the fraction of each phase which evolves with temperature and time.

The assumption used by the Reuss model is that the stresses in the two phases are the same (iso-stress), while the strains are inversely proportional to each constituent's moduli [46]. In a similar way, during the sintering of stainless-steel alloys at high temperatures, the global strain rates can be assumed to be related to the individual properties of the  $\gamma$  phase (FCC) and the  $\delta$  phase (BCC) and the amount of each phase present in the microstructure, while stresses can be regarded as homogeneously distributed within the two phases. Therefore, the individual

shear viscosities  $(\eta_{\gamma,\delta})$  and phase fractions  $(f_{\gamma},f_{\delta})$  were used to estimate the total shear viscosity  $\eta_0$  of the dual phase material during sintering by using equation (9) inspired in the Reuss model.

#### 3.3. FEM simulations and boundary conditions

The sintering model detailed in section 3 was implemented using the FEA software COMSOL Multiphysics 6.1. The CAD geometries used for the BJT printing were also imported into the software for the FEM mesh discretization. During the sintering simulations, homogeneous temperature within the components was assumed and explicitly implemented on the temperature-dependent material parameters, thus reducing the degrees of freedom of the global problem. The "tree" components CAD geometries were incorporated in the software and split into 4 regions defined by the symmetrical planes. Then, only 1/4 of the geometry was discretized and symmetry conditions were applied to the corresponding surface boundaries obtained to reduce the computational cost of the simulations. Due to the lack of symmetry the angled beam components were simulated entirely. Furthermore, the base alumina plate was added to the simulation setup as a rigid body.

The gravity forces during the simulation of BJT components were implemented as an external volumetric force that depends on the local density within the component:  $(1-\theta)\rho_{th}\vec{g}$ , where  $|\vec{g}|=9.81m/s^2$  is the gravity acceleration. This gravity forces leads to the contact between the alumina plate and BJT components, which can be simulated by using existing methods within the FEA software utilized. The penalty algorithm included in COMSOL was used for the simulation of the contact physics when indicated [48]. Nevertheless, the friction was assumed to be negligible due to the small size of the components, thus, no tangential contact forces were considered. If not indicated, the roller boundary conditions were applied in the contacting surfaces, where the out-of-plane displacement of the nodes are restricted as follows:  $u \bullet n = 0$ .

In parallel, two other variations of the normalized bulk viscosity detailed in Ref. [11] were implemented and the FEM simulation results were analyzed and compared with the ROH model proposed. The  $\psi$  model variant incorporates the normalized bulk viscosity expression proposed by Skorohod [43], which follows the function of porosity:  $\psi = 2(1-\theta)^3/3\theta$ . Besides, the  $\psi_2$  model variant contains the following normalized bulk viscosity expression:  $\psi_2 = 2(\theta_C - \theta)^3/3\theta$ , which includes a critical porosity value  $\theta_C$  as a fitting constant.

#### 3.4. Methodology for the determination of sintering model parameters

The calculation of the different material constants needed for the sintering model is a key step on the modelling framework presented in this work. The methodology developed is based on the use of experimental data collected from dilatometry experiments  $(\varepsilon,\dot{\varepsilon})$  together with the microstructural analysis (G) of the sintered samples.

The methodology for computing the material constants in the model at temperatures below the  $\delta$ -ferrite transformation is derived from the earlier study [11]. The normalized bulk viscosity constants (A,B) and the

stainless-steel material shear viscosity constants for the austenitic phase  $(A_\gamma)$  and  $Q_\gamma$  are calculated from the dilatometry experimental data by using non-linear regression algorithm levenberg-marquardt available in MATLAB [49]. A and B constants account for the influence of the porous structure characteristics to the resistance of the BJT part to the densification. The proposed  $\psi$  expression in equation (4) has the ability to adjust the effect of pore morphology at high and low porosity by adjusting A and B constants independently (as illustrated by Fig. 2), which can be done using experimental data. Also, the grain size kinetic equation constants were obtained by fitting the kinetic equation (7) to an extensive amount of grain size values measured from Ref. [11].

However, this methodology was limited to temperatures  $\leq 1300^{\circ}C$  where the effect of the delta ferrite transformation was not considered, and sintering does not reach the last stage ( $\theta < 10\%$ ) [11]. Therefore, additional experimental data within that temperature range is required for calculation of the remaining unknown material constants ( $A_{\delta}$  and  $Q_{\delta}$ ) required when the dual phase  $\gamma/\delta$  microstructure appears. These experiments should cover the widest envelope of values for the dependent variables studied (T,  $\theta$ ). Therefore, various sintering dilatometry experiments were performed with different heating rates (2, 5 and 15 °C/min) [7,8,35], as detailed in section 2. Then, the material shear viscosity can be calculated from the collected experimental data by using the following equation:

$$\eta_0 = -\frac{(1-\theta)P_L}{2\psi\dot{\theta}}\tag{10}$$

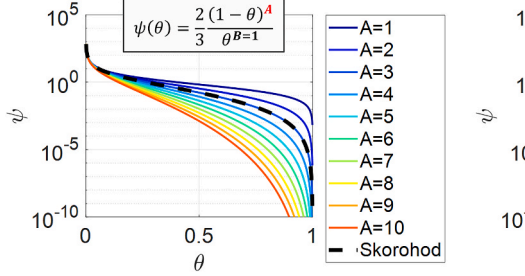
where the porosity rate  $\dot{\theta}$  is calculated from the dilatometry experimental data by following the mass conservation law.

Finally, a non-linear regression method was implemented to fit equation (9) to the data calculated from equation (10) and obtain the remaining material constants  $A_\delta$  and  $Q_\delta$ . However, the evolution of the austenite and  $\delta$ -ferrite phase fractions during sintering must be introduced in equation (9). Previous work suggested that the kinetics of the  $\delta$ -ferrite transformation does not have a large impact on the sintering behavior at moderate heating rates  $(2-15^\circ C)$  [35]. Thus, the phase fractions  $f_\gamma$ ,  $f_\delta$  obtained from thermodynamic equilibrium calculations were utilized as an initial attempt to predict the development of the dual phase material shear viscosity as a function of sintering temperature. Fig. 3 shows the phase equilibrium diagram calculated using the software JMatPro v12.4, which was used within the simulation.

#### 4. Results and discussion

#### 4.1. Calculation of material constants from dilatometry experiments

Sintering dilatometry experiments with cubical samples, as detailed in section 2, were used to collect data for the calculation of the sintering model constants. Table 3 shows the density and shrinkage results from the data collected before and after dilatometry. In general, the samples were densified up to 96–98 % density, with the sample subjected to the longest dwell time (150 min) reaching the highest density of 98.1 %. Sintered shrinkages along the building direction (Z axis) were a



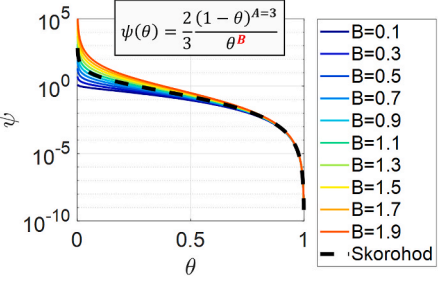


**Fig. 2.** Visualization depicting the impact of constants A and B on the evolution of  $\psi$  in relation to porosity.

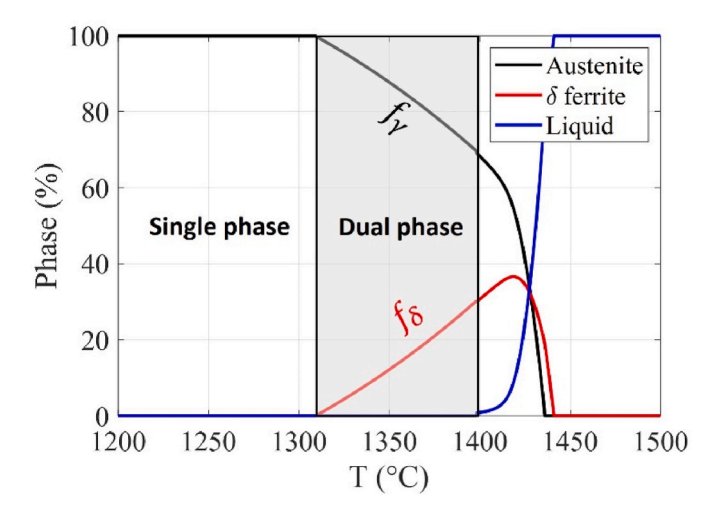


Fig. 3. Phase equilibrium calculated by JMatPro v12.4. for stainless-steel using the chemical composition from Table 1.

**Table 3**Cube's samples density and shrinkages subjected to dilatometry sintering.

				•		
Sample ID	$ ho_{pre-sintered}$ (geometry-based)	$\boldsymbol{arepsilon}_{x}$	$oldsymbol{arepsilon}_y$	$oldsymbol{arepsilon}_z$	$ ho_{sintered}$ (geometry-based)	$ ho_{sintered}$ (Archimedes)
HR2- 1370- 60	57.0 %	15.5 %	16.0 %	17.1 %	95.0 %	96.2 %
HR5- 1370- 60	56.5 %	16.0 %	16.5 %	17.9 %	96.0 %	97.5 %
HR5- 1370- 150	57.3 %	16.0 %	16.7 %	17.5 %	97.0 %	98.1 %
HR15- 1370- 60	57.2 %	15.8 %	16.2 %	17.1 %	95.4 %	97.0 %

maximum of  $\sim 1.5$  % larger than the other directions. Despite the minor anisotropy noted during the sintering of these 316L BJT samples [11], it was necessary to incorporate its influence on the densification calculation from dilatometry to prevent unrealistically high densities exceeding full densification, as depicted in Fig. 4 (a). Therefore, anisotropic factors

obtained from dimensional shrinkage measurements of sintered cubical samples were introduced for the calculation of  $\dot{\theta}$  and  $\theta$  from the dilatometry data shown in Fig. 4 (b).

The methodology detailed previously in section 3.3 was followed for the calculation of the required material constants for the sintering model. Dilatometry and experimental data collected from Ref. [11] were re-processed to determine the material constants  $A_{\gamma}$ ,  $Q_{\gamma}$ , A and B. Then, the data shown in Fig. 4 (b) were used to fit the constants  $A_{\delta}$  and  $Q_{\delta}$  by using non-linear regression method. In parallel, the same methodology was followed for the model variants detailed in the previous section 3.3. The complete sintering model constants obtained following this methodology are depicted in Table 4.

The experimental shear viscosity  $\eta_0$  in Fig. 5 was calculated by introducing dilatometry data (see Fig. 4 b) and grain kinetics (equation (7) with constants from Ref. [11]) into equation (10). A surface energy of 1.2 J/m² was used for the 316L alloy [50]. Then, the viscosity evolution with the temperature described by equation (9) was calculated using the constants from Table 4 and plotted to show the correlation with the experimental data for each case. The  $\eta_0$  evolution will determine the densification and shape deformation behavior during the sintering simulations, which results will be shown and discussed in the next sections.

#### 4.2. Sintering experiments of complex components with overhangs

The final sintered BJT tree components are shown in Fig. 6. Significant volume shrinkage and shape distortion, induced by the gravitational forces, can be observed on these components. The component with thinner overhangs of 2 mm undergoes the larger shape deformation, when compared to the 3 mm thickness component. Naturally, the longest beams undergo the largest bending deformation during the sintering process on the tree samples. Note that beam deformations are substantial but low enough to avoid the collapse of the geometry (i.e. contact between the deformed parts and the supporting alumina plate and/or self-contact of the deformed geometry). This is important when the experiments aim for the verification of the simulation results since the collapse of the component would hinder to some extent the geometry deformation during sintering. Also, the geometry (STL file) obtained from the X-Ray computed tomography characterization (XCT) of the sintered tree components can be observed in Fig. 6. These geometries will be used for the verification of the model by running a detailed comparison with the simulation results in section 4.3.

The density of the BJT components at the green state (before sintering) and the sintered state are detailed in Table 5. The green density

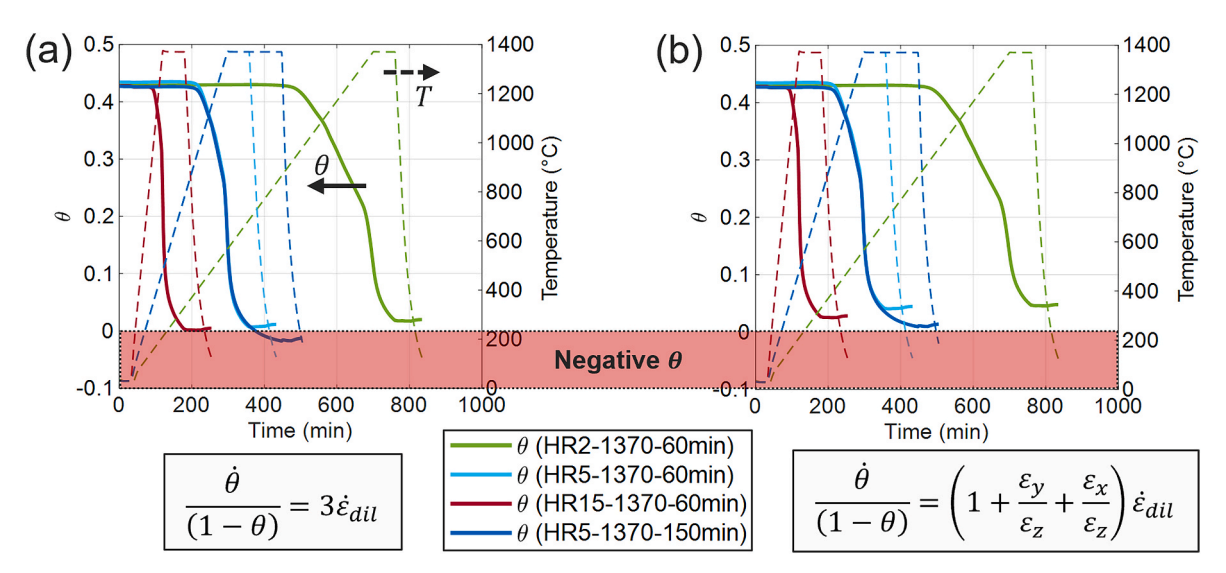


Fig. 4. Porosity evolution derived from dilatometry data: (a) assuming same shrinkage along all directions, (b) scaling the dilatometry data with shrinkage ratios.

**Table 4**Sintering model constants for each model case studied.

	$A_{\gamma}$ $[Pa \bullet s / K]$	$\begin{matrix} A_{\delta} \\ [Pa \bullet s / K] \end{matrix}$	$Q_{\gamma} [kJ/mol]$	$Q_{\delta}$ [kJ/mol]	Α	В	$ heta_c$
ROH model	2.509	1.201E-18	215.7	738.4	11.160	0.693	_
$\psi_2$ model	3.112	2.056E-19	219.2	772.7	-	-	0.505
ψ model	41.610	0.423	149.7	160.8	-	-	-

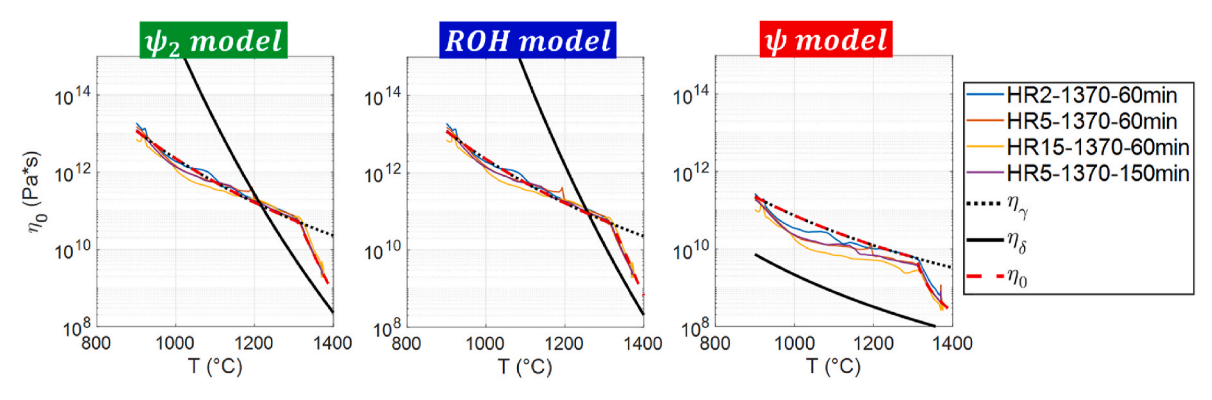


Fig. 5. Viscosity evolution as a function of sintering temperature. The viscosity derived from experimental data and calculated from the fitted equation (9) are shown.

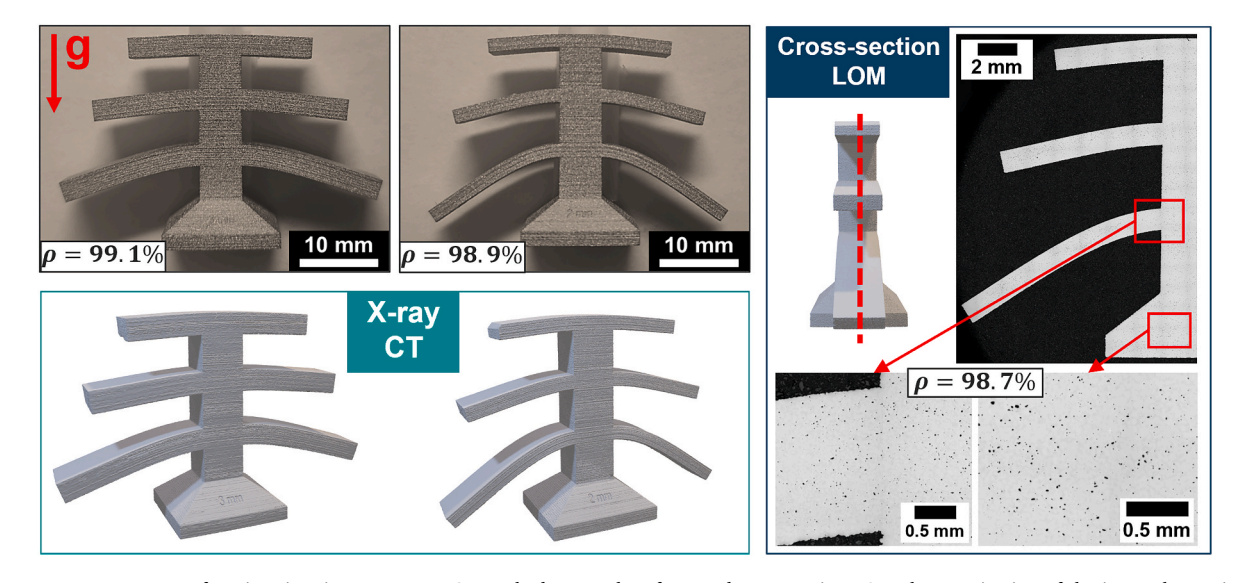


Fig. 6. Tree BJT components after sintering: images, X-Ray CT meshed external surface, and cross-section LOM characterization of the internal porosity of the 2 mm tree.

**Table 5**Green and sintered density of the BJT components.

Sample	Green density (Geometry- based)	Sintered density (Archimedes)
Tree 2 mm	56.3 %	98.9 %
Tree 3 mm	56.4 %	99.1 %
90-60-30_10 mm	56.5 %	98.5 %
90-60-30_12 mm	55.6 %	98.4 %
75-45-15_10 mm	54.5 %	97.7 %
75–45–15 <sub>_</sub> 13 mm	54.3 %	97.4 %

slightly fluctuates between 54.3 % and 56.5 % for the different

components. This could be caused by the impact of different components geometrical features on the printing accuracy. Also, the use of the component CAD as source for the volume calculation and the experimentally measured weight to calculate the density could lead to the small discrepancies observed. These discrepancies are slightly larger between the components with angled overhangs. Nonetheless, they are close to the values experimentally measured for the green cubes presented in Table 3. High final sintered densities >97 % were achieved for all the components studied, with a similar trend showing slightly higher sintered densities on the tree components. The internal porosity structure was characterized by the LOM image analysis of cross-sections and can be observed in Fig. 6. In general, homogeneous pore distribution was observed within the cross-section of the tree samples.

The sintered BJT angled beams components are displayed in Fig. 7 Similar volume shrinkage but significantly less shape distortion can be observed on these components, compared to the tree samples in Fig. 6.

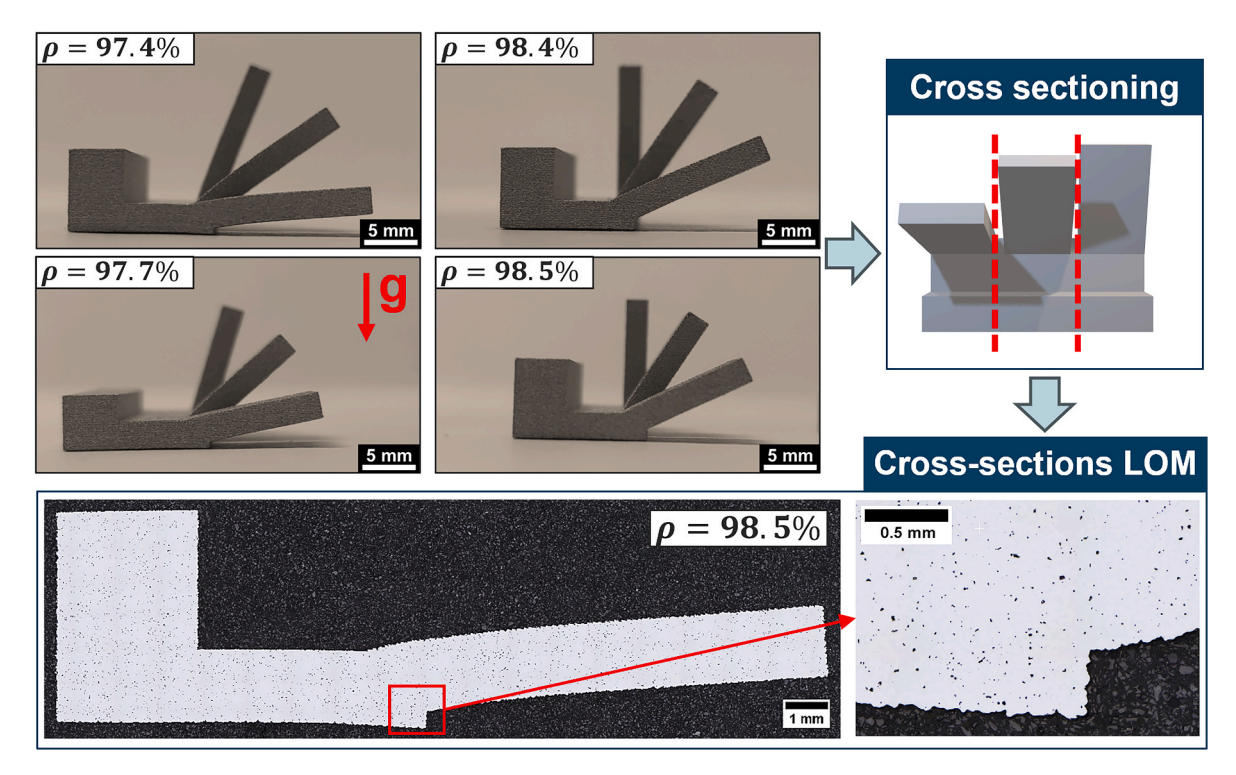


Fig. 7. Angled beams BJT components after sintering: images and cross-section LOM characterization of the internal porosity of the 13 mm beam at 15° angle.

This is probably due to the smaller length of the beams together with the progressive decrease on the beam's angles compared with the orthogonal beam designed on the tree components. The beams at a lower angle of 15° respect to the horizontal direction and the longest length of 13 mm experience the largest shape deformation. At the same time, the vertical beams do not experience a noticeable shape deformation during sintering and just undergo shrinkages related to densification. Like in the sintered trees, the angled beam components do not collapse during sintering. As an illustration, Fig. 7 shows the internal porosity structure characterized by LOM image analysis of the cross-sectioned 15° - 13 mm length beam. In general, the pore distribution within the cross-section of these samples also appears to be reasonably homogeneous. Further analysis of the LOM images will be performed for the comparison against the simulation results in the following section 4.4.

The microstructure at the end of the sintering process was also characterized using EBSD. Fig. 8 shows an EBSD phase map obtained from the bottom region of the 2 mm tree component (tree base). A dual phase microstructure consisting of 97.6 % FCC (austenite) matrix along with a 1.9 % of dispersed BCC (delta-ferrite) was distinguished. Typically, the formation of delta-ferrite takes place along the interfaces as grain boundaries and pore surfaces, which agrees with the morphology and location of the BCC phase in Fig. 8. However, only a residual amount of the delta-ferrite is retained after slow cooling to room temperature.

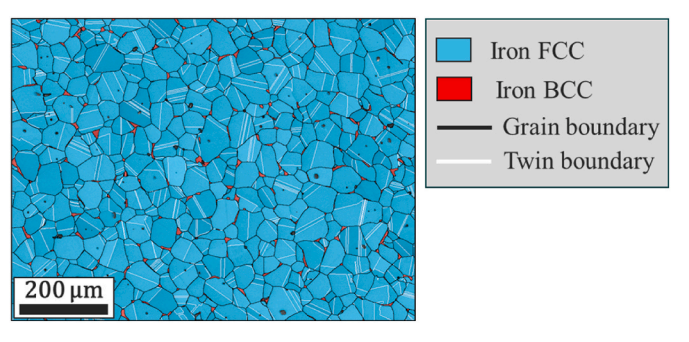


Fig. 8. EBSD phase map of the sintered microstructure.

When it comes to the grain size, a mean circle diameter of 36.3  $\mu m$  and 6.45  $\mu m$  was obtained for the FCC and BCC grains in the phase map, respectively.

#### 4.3. Sintering simulations of tree-shape components under gravity: Rios-Olevsky-Hryha (ROH) sintering model validation

Figs. 9 and 10 depict the final tree component's sintered geometry and density from the simulation results of the ROH model and the other models. In general, the simulated three geometries show larger shape deformation of the 2 mm tree (Fig. 9) when compared to the 3 mm tree (Fig. 10), similar to the experimental results shown in Fig. 6. A direct comparison between different model results is shown in Fig. 9 (a) and Fig. 10 (a), where the  $\psi$  model shows the largest shape deformation caused by gravitational forces, collapsing during sintering. The alternative models demonstrate varying degrees of deformation, as evident in the vertical displacement of the bottom overhang tip shown in Fig. 9 (c) and Fig. 10 (c). Notably, the ROH model exhibits an intermediate level of deformation during sintering compared to the others. Throughout the simulation, most of the overhang deflection occurs during the dwell time at the peak temperature of 1370 °C, even though the average density has already exceeded 90 %. This features the substantial influence of the shear viscosity value on the gravitationalinduced geometric distortions observed throughout the hightemperature sintering range. Notably, at the dwell temperature, the  $\eta_0$ value for the model  $\psi$  was one order of magnitude lower compared to the others, as shown in Fig. 5. Finally, the complete final solution obtained by the application of symmetry to the FEM results on the different models are shown in Fig. 9(d-f) and Fig. 10(d-f) for the 2 mm tree and 3 mm tress geometries, respectively.

Looking at the sintered density of the components, the  $\psi$  model predicted a slightly higher density of  $\sim$ 99.9 % compared with the other model's results of  $\sim$ 99.0 % sintered density. Also, the density evolution during sintering was different, where the ROH and  $\psi_2$  models show similar behavior. This is related to the different forms of the normalized bulk viscosity expressions as discussed in a previous study [11]. In this previous work, the expressions with one or more fitting constants were

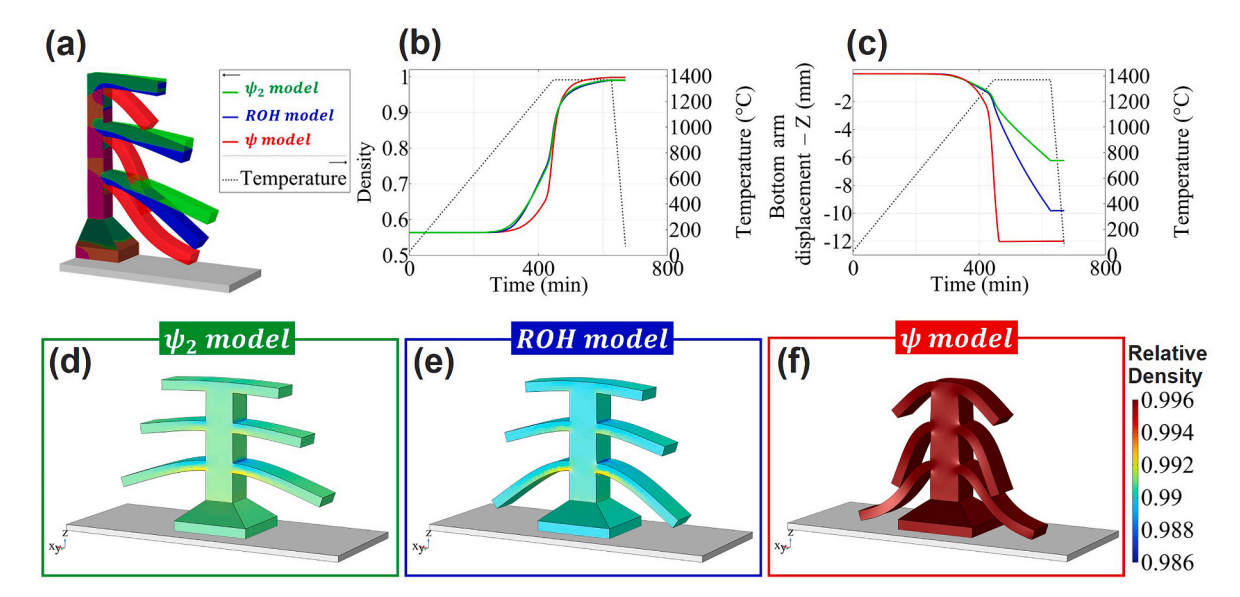


Fig. 9. Sintering simulation results for the 2 mm tree geometry. (a) Comparison of the final geometry obtained for the different models used. (b) Averaged density evolution within the component during the simulation. (c) Vertical displacement of the bottom overhang tip during the sintering simulations. (d–e) Reconstructed solution of the final sintered geometry for the different models used, where the component colormap represents the final density.

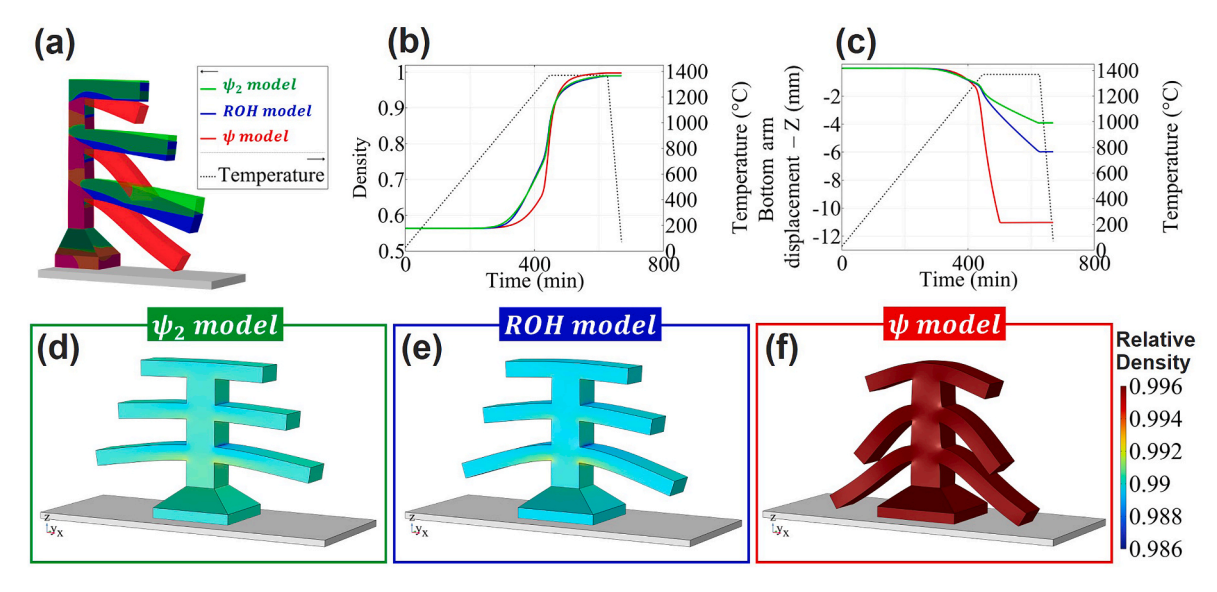


Fig. 10. Sintering simulation results for the 3 mm tree geometry. (a) Comparison of the final geometry obtained for the different models used. (b) Averaged density evolution within the component during the simulation. (c) Vertical displacement of the bottom overhang tip during the sintering simulations. (d–e) Reconstructed solution of the final sintered geometry for the different models used, where the component colormap represents the final density.

more accurate when describing the densification behavior for the diverse temperature-time conditions studied. Furthermore, the ROH and  $\psi_2$  models revealed a particular density distribution, with slightly higher density region located in the bottom of the overhangs compare with the top region (see Fig. 9(d and e) and Fig. 10(d and e)). This effect can be related to the stress distribution caused by the gravitation forces, where compression forces are located on the bottom contributing to the sintering stresses and increasing the local densification while tension stresses at the top diminish the densification. However, this effect is very minimal and induced a difference of less than 1 % on the final density between these regions. This result agrees with the experimental general homogeneous pore distribution (see Fig. 6), where such small inhomogeneities would be impossible to be identified.

After the simulation results were obtained and analyzed, the last time-step solution was directly compared with the results obtained from the XCT characterization results of sintered tree geometries shown in

Fig. 6. This comparison was performed by using the 3D point cloud (and triangular mesh) processing open-source software CloudCompare (version 2.12). The mesh derived from the XCT experiment and a refined mesh from the FEM simulation result were aligned together and the distances between them were computed. Fig. 11 shows the results of this analysis for each model results of the two tree geometries, where the XCT is shown as a translucent gray mesh and the simulation mesh is colored according to the 3D distance measurements results. In general, it is noticeable that the  $\psi_2$  model tends to underestimate, while the  $\psi$ model tends to overestimate the bending distortion of the 2 mm and 3 mm tree overhangs. Note that the distance between the experiment and simulation meshes is computed from the closest mesh points, as it can be observed in Fig. 11 (c) and (f). Therefore, the actual distortions are much larger than the computed distances for these cases. Finally, the ROH model comparison with the experimental XCT results in Fig. 11 (b) and (e) shows a remarkably good agreement. The largest deviation of 0.56

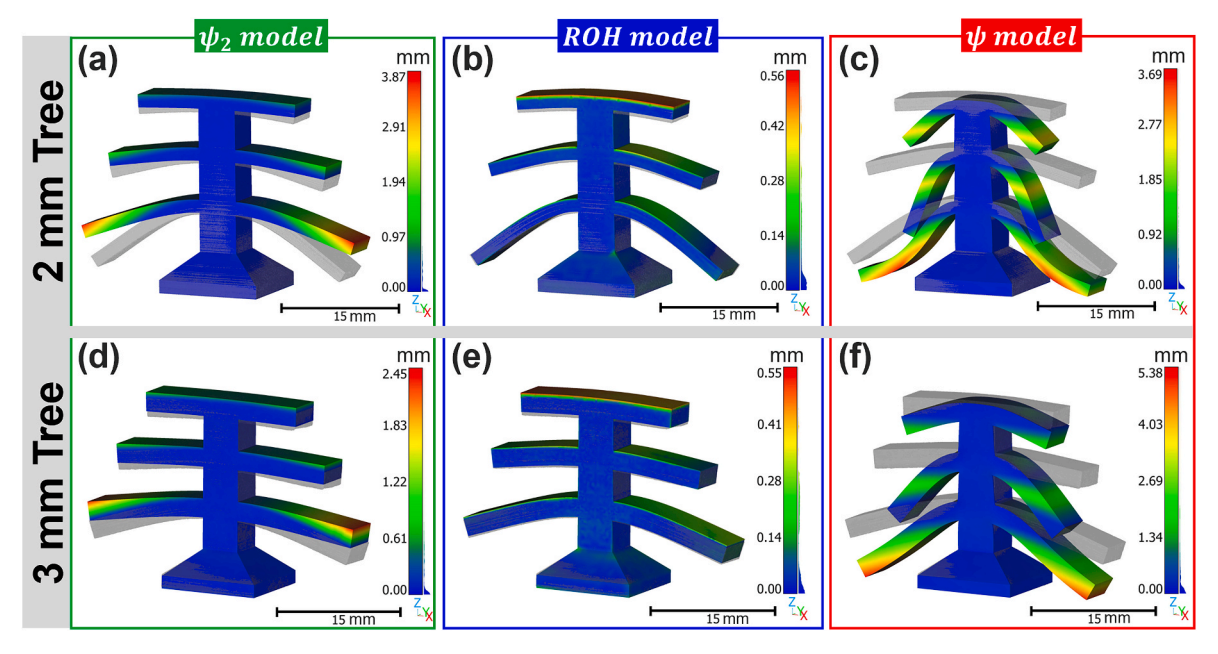


Fig. 11. Comparison between the sintered trees experimental XCT characterization and the final simulation results: (a–c) 2 mm tree geometry and (a–c) 3 mm tree geometry compared against the different model's results. The experimental XCT derived mesh is shown as a translucent gray mesh. The calculated distances are overlayed as a colormap on the final simulation result mesh for each case.

mm and 0.55 mm was obtained from the 2 mm and 3 mm tree's results respectively. This independence of the geometry on the accuracy of the simulation suggests the good performance of the ROH model implemented. It is interesting to notice that the maximum deviation was observed at the top surface of the geometry instead of being located at the point of maximum beam deflection. This may be associated with slight anisotropy in shrinkages during the sintering of the BJT components, as evidenced by the sintering results of the cubical sample presented in Table 3. The anisotropic shrinkages observed in the studied samples are significantly smaller when compared to those reported in previous studies [8,51-54], resulting in minimal deviations attributed to this effect. Therefore, the isotropic ROH sintering model proposed here should be used with precaution when highly anisotropic shrinkages are observed in BJT components. In future studies, the expansion to the anisotropic case will enable further improvements on the accuracy of the model presented here. The results discussed in this section were considered as a validation of the ROH sintering model framework detailed in section 3, which will be further used in the following sections of this work.

# 4.4. Sintering simulation of angled overhang components: analysis of different boundary conditions on the simulation of components under gravity

The second set of geometries studied are comprised by various angled beam components which included beams at different angles and lengths, as detailed in section 2. The sintering simulations were done using the original CAD files and the developed ROH model, which was verified in the previous section 4.3. Note that these geometries do not have any plane of symmetry, thus the complete geometry was discretized and used for the FEM calculations. Then, two different boundary conditions (as detailed in section 3.3) were implemented and tested for the geometry with the longest beams of 13 mm in Fig. 1 (c), which is expected to have the largest shape deformation during the sintering simulations.

Fig. 12 shows the comparison between the LOM cross-section image of the sintered component (see Fig. 7) and the equivalent virtual cross-section of the result at the end of the sintering simulations. Fig. 12 (a) displays the simulation results with the roller boundary condition implemented, while Fig. 12 (b) shows the simulation results with the implemented contact boundary condition. These comparisons reveal a slight difference in the component shape deformation during the sintering simulations depending on the employed boundary condition. The

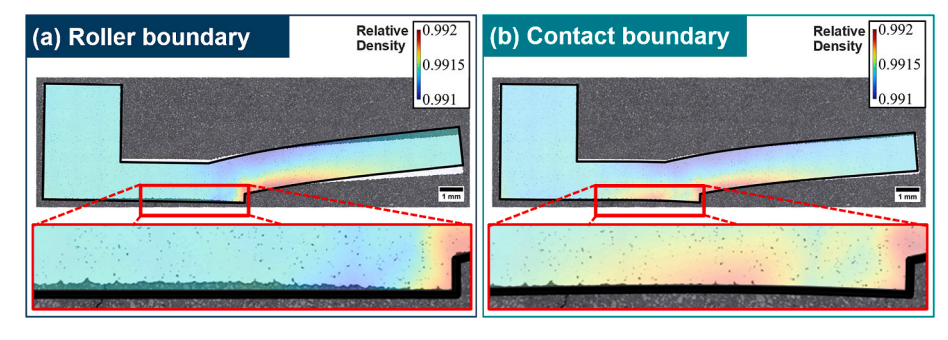


**Fig. 12.** Experimental LOM image of the 13 mm length and 15° angle beam cross-section with the corresponding simulation results overlayed (external surface as black line and colored internal density distribution). Simulation with (a) roller boundary condition and (b) contact physics included between the contact surfaces (component and support plate).

implementation of rolling conditions on the bottom surface imposes a restriction on the surface normal displacements, as observed in Fig. 12 (a). Simulating contact conditions allows for the normal displacement opposite to the contacting surface, resulting in a slight bending of the bottom surface caused by the global equilibrium between internal stresses and external forces (i.e., contact forces and gravity). Furthermore, the level of bending deformation in the angled beam during sintering was influenced, aligning more closely with experimental observations. The comparisons in Fig. 12 highlight a more accurate sintering predictions when incorporating contact conditions in the simulation of asymmetrical geometries during the sintering of BJT components under gravity. Accordingly, the subsequent sections present simulation results corresponding to the implementation of contact boundary conditions.

Fig. 13(a–d) shows the outcome of the sintering simulation at the final time step for the different angled beam geometries. The gray outline of the original component's CAD files provides a reference to perceive the extent of volume shrinkage and shape distortion in the sintered geometries. In general, the degree of beam bending increases with the beam length and diminishes with an increase in the angle relative to the horizontal direction. The averaged sintered density attained by the simulations is >99 %, while some minor differences on the green and sintered density were observed between the different components (depicted in Table 5). The density distribution observed within the components in Fig. 13(a–d) indicates a slightly higher density in the lower regions of the beams, where compressive stresses prevail. Conversely, regions experiencing tensile stresses at the top of the beams exhibit lower sintered density. This observed effect aligns with the simulation results for tree geometries discussed in section 4.3.

As previously discussed, incorporating contact boundary conditions in the sintering simulation of angled beam components leads to the distortion of the bottom surface. Fig. 14 (a) illustrates the main outcomes of the use of contact boundary conditions: the bottom surface vertical displacement and contact pressure distribution. Specific regions of the bottom surface lose contact with the supporting plate during the simulation, resulting in a particular distribution of vertical separation and contact pressure between these two components. The central region of the bottom surface aligned with the lowest angle beam exhibits the largest vertical displacement, while the corners maintain contact with the supporting plate and exhibit the highest contact pressure. This phenomenon arises from the concentration of the component's weight on these reduced contact areas caused by the deformation of the bottom surface.

Additionally, Fig. 14(b-e) shows the vertical displacement of the

bottom surface for the different geometries used in the sintering simulations. In general, the same behavior is observed, where the bending separation increases from the higher beam angle to the regions closer to the lower angle beams. Also, the global extent of vertical displacements increases for the components with larger beam lengths and lower angles. This phenomenon can be elucidated by the force balance of the beams, acting as a lever, and generating larger internal stresses when the mass center of the beam shifts farther from the component's base in contact with the supporting plate. Accordingly, the component with 13 mm beams at angles of  $15^{\circ}$ ,  $45^{\circ}$  and  $75^{\circ}$  shows the maximum surface displacement of  $63.1~\mu m$ , as observed in Fig. 14 (b). The lowest maximum displacement of  $15.3~\mu m$  is shown by the simulation of the component with 10 mm beams at angles of  $30^{\circ}$ ,  $60^{\circ}$  and  $90^{\circ}$ , as observed in Fig. 14 (e).

These results reveal the outcome of including the contact boundary conditions within the simulation of specific geometries, particularly when the external forces balance can generate stress distributions leading to the deformation of the bottom surface in contact with the supporting plate. Despite the low extent of the surface vertical displacement ( $\sim\!63~\mu m$ ), it was clearly observed within the LOM cross-section image analysis, and its comparison with the simulation including the contact boundary shows the best agreement in Fig. 12. However, the inclusion of contact physics in the simulation introduces significant non-linearity, making the FEM model more sensitive to the discretization process and prone to numerical instabilities. Also, the average computational time of the simulations increases by a factor of 4 due to the extensive contact physics calculations carried out every time-step.

Fig. 15 shows the simulation cross-sections results (colored by relative density value) overlayed on the experimental cross-section (obtained as illustrated in Fig. 7) of the different angled beams of the 15-45-75\_13 mm component. The model demonstrates accurate predictions for both the volume shrinkage and shape distortion of the different angled beams. Interestingly, the beam with the most significant bending deformation shows a better agreement with the experimental sintered shape than the other two beams, despite experiencing the least shape deformation. Regarding the internal density distribution, simulations revealed areas with higher relative density located in the bottom region of the beams, where compressive stresses are induced by the external gravitational forces. The same effect was observed in the simulation results of the tree-shape components. A zoom into the root area of the lowest angle beam in Fig. 15 reveal the characteristic density distribution and its comparison with the pore distribution within the experimental cross-section. However, the difference between the lower and

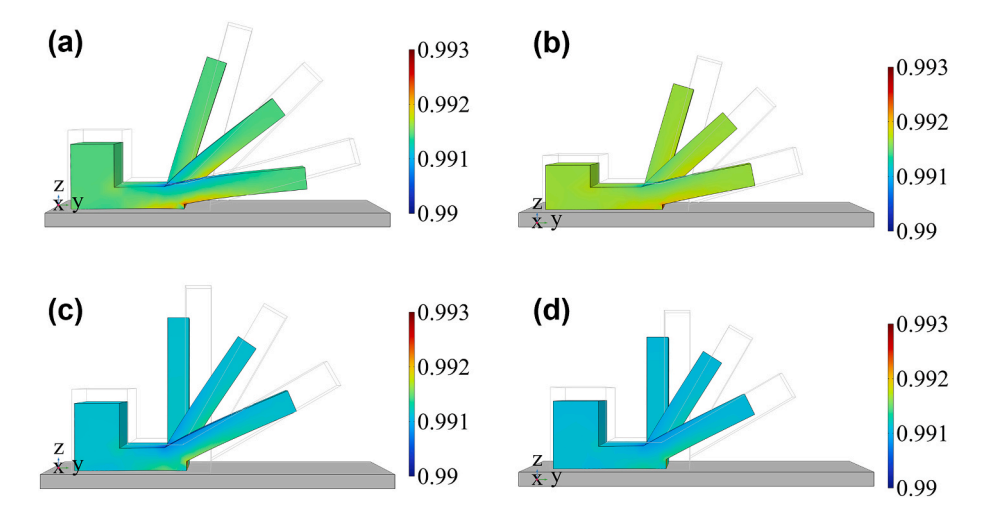
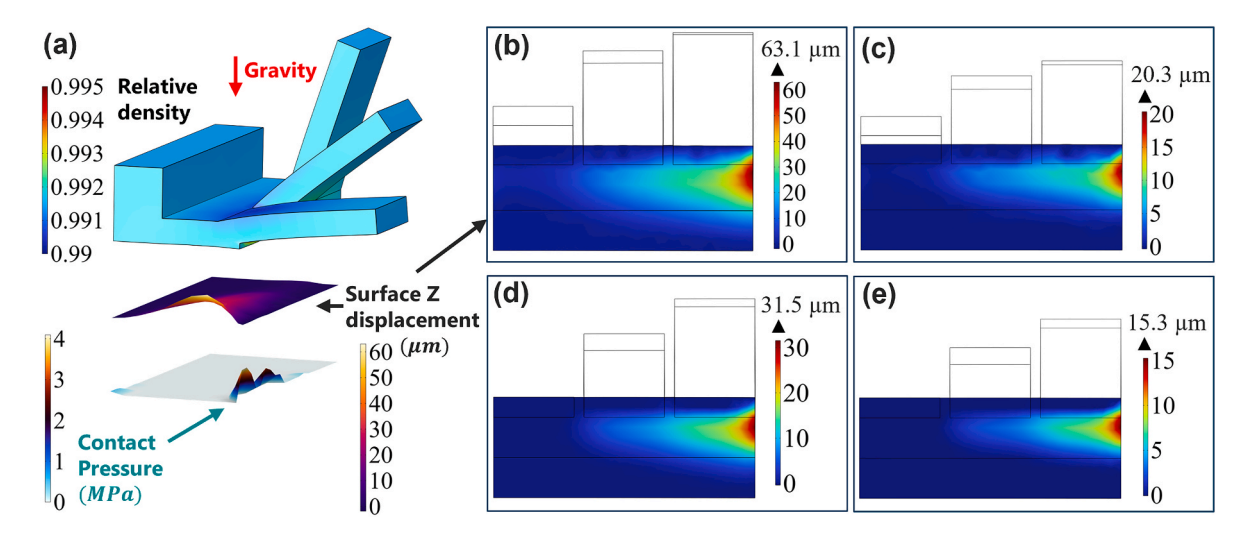
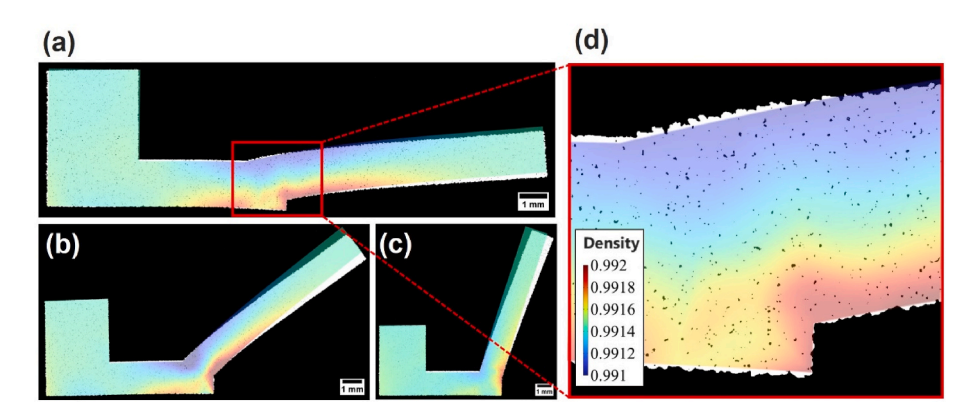


Fig. 13. Simulation results corresponding to the final time-step of the different angled beam components studied: (a) 75-45-15\_13 mm, (b) 75-45-15\_10 mm, (c) 90-60-30\_12 mm, (d) 90-60-30\_10 mm. The initial CAD geometry lines are plotted in light gray, and the final relative density is plotted following the colormap legend.



**Fig. 14.** Sintering simulation of the angled beam components incorporating the contact physics. (a) 3D plot of sintered geometry together with 2D plots of the bottom surface's Z displacement and contact pressure of the 75-45-15\_13 mm component. The 2D plots of the bottom surface Z displacement is plotted for the components: (b) 75-45-15\_13 mm, (c) 75-45-15\_10 mm, (d) 90-60-30\_12 mm, (e) 90-60-30\_10 mm.



**Fig. 15.** Comparison of LOM cross-section images with the corresponding virtual cross-section of the sintering simulation results. The different 13 mm angled beams were compared: (a) 15°, (b) 45° and (c) 75°. (d) shows a zoom in the root region of the 15° beam.

higher density area was negligible ( $\sim$ 0.1 %) and extremely difficult to differentiate experimentally from 2D cross-sections. Fig. 16(a–c) display the same comparison between experiment and simulation cross-sections for the rest of angled beam components analyzed during this study. A

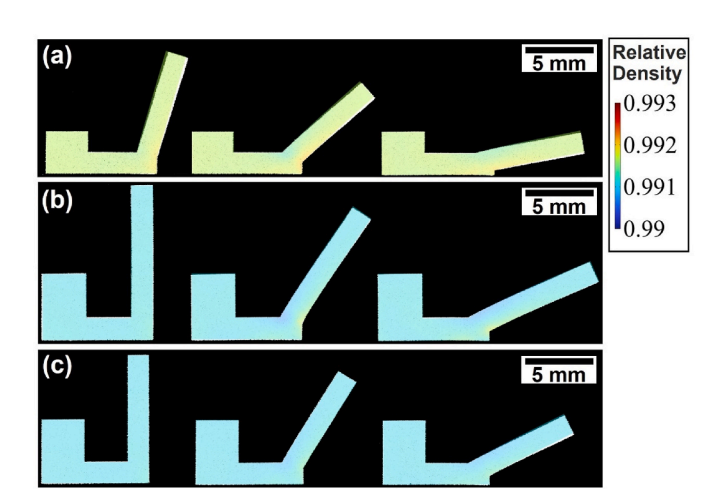


**Fig. 16.** Comparison of LOM cross-section images of the different angled beams with the corresponding virtual cross-section of the sintering simulation results: (a) 75-45-15\_10 mm, (b) 90-60-30\_12 mm, (c) 90-60-30\_10 mm component.

remarkable accuracy of the modelling results regarding the components shrinkage and sintered geometry can be observed. Also, any internal density distribution within the components is minimal and cannot be distinguished by the experimental characterization performed.

#### 5. Conclusions

A new modelling framework for the prediction of BJT stainless-steel components evolution during the sintering process was developed, including the phenomenological Rios-Olevsky-Hryha sintering model and the methodology for the identification of the material constants. The sintering model incorporates fitting constants to account for the variations linked to the features of the pore network morphology, influenced by particle characteristics, BJT system, and printing parameters. This enables the model's potential application regardless of the printer or powder size/shape utilized. Besides, the material shear viscosity explicitly accounts for the impact of the delta-ferrite phase transformation occurring when sintering stainless-steel at high temperatures close to the solidus point. This approach paves the path for future integration of the ROH sintering model with thermodynamic calculations, allowing for the consideration of variations in stainless-steel alloy composition and their impact on sintering behavior.

The model was solved using FEA tool and validated against detailed experimental data collected from the sintering of BJT components. The tree components simulations revealed the excellent performance of the

model when predicting sintering volumetric shrinkages and gravity induced shape deformation. The ROH model showed a maximum deviation of 0.56 mm and 0.55 mm from the 2 mm and 3 mm tree's results respectively. Other variations of the model were analyzed, where the  $\psi_2$ model tends to underestimate and the  $\psi$  model tends to overestimate the geometrical sintering deformation, mainly influenced by the fitted material shear viscosity. Besides, the angled beam components simulations revealed the effect of using two different boundary conditions on the surface in contact with the supporting plate. Roller boundaries are more computationally efficient and can accurately predict sintering when no bottom surface distortions are expected. The use of contact physics in the simulations by using the penalty method increases the computational cost but allows for a more accurate prediction of the shape distortions during sintering. Therefore, considering these factors allows for the selection of adequate boundary conditions during the setup of the simulation and the optimization of the problem.

Further research focused on the developed framework is required to account for some of the characteristics of the BJT sintering process which were simplified in this study. The expansion to the anisotropic sintering behavior on the continuum scale would become highly relevant when using the model to simulate components printed with other powders and/or BJT printer that may induce larger sintering shrinkage anisotropy. Another effect that was simplified in this study was the influence of the friction between the supporting plate and the BJT components. The friction can be simulated using Coulomb's friction law, but the identification method of the necessary friction coefficients should be added to the simulation framework and verified. Furthermore, the heat transfer physics within the BJT components could be added to the simulation for more realistic simulations. Adding these effects (i.e. friction and heat transfer) to the simulation will become more relevant with the increase in the size and weight of the components being sintered. However, they will have a detrimental impact on the computational costs of the simulations. Therefore, a meticulous analysis of the tradeoff between the prediction accuracy improvement and the rise in simulation complexity and cost should be carried out.

#### CRediT authorship contribution statement

Alberto Cabo Rios: Conceptualization, Data curation, Formal analysis, Investigation, Methodology, Software, Writing – original draft. Mats Persson: Formal analysis, Investigation, Resources. Eduard Hryha: Conceptualization, Formal analysis, Supervision, Writing – review & editing. Eugene Olevsky: Conceptualization, Formal analysis, Supervision, Writing – review & editing.

#### Declaration of competing interest

The authors declare that they have no known competing financial interests or personal relationships that could have appeared to influence the work reported in this paper.

#### Acknowledgements

This work was conducted in the framework of the Centre for Additive Manufacturing – Metal (CAM²), supported by the Swedish Governmental Agency of Innovation Systems (Vinnova). The support of the US National Science Foundation (Collaborative Grants DMREF-2119832 and DMREF-2119833) is gratefully appreciated. The authors gratefully acknowledge the contributions of Lauren Enghien and Bieke Smeuninx to the X-Ray CT characterization of the BJT components at Nikon Metrology Europe NV.

#### References

- [1] S. Ford, M. Despeisse, Additive manufacturing and sustainability: an exploratory study of the advantages and challenges, J. Clean. Prod. 137 (2016) 1573–1587, https://doi.org/10.1016/j.jclepro.2016.04.150.
- [2] K.V. Wong, A. Hernandez, A review of additive manufacturing, ISRN Mechanical Engineering 2012 (2012) 1–10, https://doi.org/10.5402/2012/208760.
- [3] A. Lores, N. Azurmendi, I. Agote, E. Zuza, A review on recent developments in binder jetting metal additive manufacturing: materials and process characteristics, Powder Metall. 62 (2019) 267–296, https://doi.org/10.1080/ 00325899.2019.1669299.
- [4] ASTM International, ISO/ASTM52900-21 Standard Terminology for Additive Manufacturing – General Principles – Terminology, ASTM International, West Conshohocken, PA, 2021, http://www.ciri.org.nz/nzrma/technologies.html.
- [5] R.K. Enneti, S.J. Park, R.M. German, S.V. Atre, Review: thermal debinding process in particulate materials processing, Mater. Manuf. Process. 27 (2012) 103–118, https://doi.org/10.1080/10426914.2011.560233.
- [6] N. Lecis, M. Mariani, R. Beltrami, L. Emanuelli, R. Casati, M. Vedani, A. Molinari, Effects of process parameters, debinding and sintering on the microstructure of 316L stainless steel produced by binder jetting, Mater. Sci. Eng. 828 (2021) 142108, https://doi.org/10.1016/j.msea.2021.142108.
- [7] A. Cabo Rios, E. Hryha, E. Olevsky, P. Harlin, Sintering anisotropy of binder jetted 316L stainless steel: part II – microstructure evolution during sintering, Powder Metall. 65 (2022) 283–295, https://doi.org/10.1080/00325899.2021.2020486.
- [8] A. Cabo Rios, E. Hryha, E. Olevsky, P. Harlin, Sintering anisotropy of binder jetted 316L stainless steel: part I – sintering anisotropy, Powder Metall. 65 (2022) 273–282, https://doi.org/10.1080/00325899.2021.2020485.
- [9] Y. Wang, Y.F. Zhao, Investigation of sintering shrinkage in binder jetting additive manufacturing process, Procedia Manuf. 10 (2017) 779–790, https://doi.org/ 10.1016/j.promfg.2017.07.077.
- [10] Y. Bai, G. Wagner, C.B. Williams, Effect of particle size distribution on powder packing and sintering in binder jetting additive manufacturing of metals, Journal of Manufacturing Science and Engineering, Transactions of the ASME 139 (2017) 1–6. https://doi.org/10.1115/1.4036640.
- [11] A. Cabo Rios, E. Olevsky, E. Hryha, M. Persson, R.K. Bordia, Analytical models for initial and intermediate stages of sintering of additively manufactured stainless steel, Acta Mater. 249 (2023) 118822, https://doi.org/10.1016/j. actamat 2023 118822
- [12] H. Blunk, A. Seibel, Toward a design compendium for metal binder jetting, Innovative Product Development by Additive Manufacturing 2021 (2023) 39–48, https://doi.org/10.1007/978-3-031-05918-6 3.
- [13] H. Blunk, A. Seibel, Design guidelines for metal binder jetting, Progress in Additive Manufacturing (2023), https://doi.org/10.1007/s40964-023-00475-y.
- [14] M. Zago, M. Perina, I. Cristofolini, Preliminary design method accounting for shape distortion in metal Binder jetting parts: a case study, Lecture Notes in Mechanical Engineering (2023) 925–936, https://doi.org/10.1007/978-3-031-15928-2-81/ TABLES/4
- [15] S. Sadeghi Borujeni, G.S. Saluja, V. Ploshikhin, Compensation of sintering deformation for components manufactured by metal binder jetting using numerical simulations, Rapid Prototyp. J. (2022), https://doi.org/10.1108/RPJ-06-2022-0181
- [16] G.W. Scherer, S.M. Rekhson, Viscoelastic-elastic composites: I, general theory, J. Am. Ceram. Soc. 65 (1982) 352–360, https://doi.org/10.1111/J.1151-2916.1982.TB10470.X.
- [17] E.A. Olevsky, Theory of sintering: from discrete to continuum, Mater. Sci. Eng. R Rep. 23 (1998) 41–100, https://doi.org/10.1016/S0927-796X(98)00009-6.
- [18] J. Song, T. Barriere, B. Liu, J.C. Gelin, G. Michel, Experimental and numerical analysis on sintering behaviours of injection moulded components in 316L stainless steel powder, Powder Metall. 53 (2010) 295–304, https://doi.org/10.1179/ 00258008334212
- [19] R.K. Bordia, S.J.L. Kang, E.A. Olevsky, Current understanding and future research directions at the onset of the next century of sintering science and technology, J. Am. Ceram. Soc. 100 (2017) 2314–2352, https://doi.org/10.1111/jace.14919.
- [20] J.A. Alvarado-Contreras, E.A. Olevsky, A.L. Maximenko, R.M. German, A continuum approach for modeling gravitational effects on grain settling and shape distortion during liquid phase sintering of tungsten heavy alloys, Acta Mater. 65 (2014) 176–184, https://doi.org/10.1016/j.actamat.2013.10.059.
- [21] J.A. Alvarado-Contreras, E.A. Olevsky, R.M. German, Modeling of gravity-induced shape distortions during sintering of cylindrical specimens, Mech. Res. Commun. 50 (2013) 8–11, https://doi.org/10.1016/j.mechrescom.2013.02.007.
- [22] M. Braginsky, V. Tikare, E. Olevsky, Numerical simulation of solid state sintering, Int. J. Solid Struct. 42 (2005) 621–636, https://doi.org/10.1016/j. iisolstr 2004 06 022.
- [23] R.M. McMeeking, L.T. Kuhn, A diffusional creep law for powder compacts, Acta Metall. Mater. 40 (1992) 961–969, https://doi.org/10.1016/0956-7151(92) 90073-N.
- [24] Z.-Z. Du, A.C.F. Cocks, Constitutive models for the sintering of ceramic components—I. Material models, Acta Metall. Mater. 40 (1992) 1969–1979, https://doi.org/10.1016/0956-7151(92)90183-F.
- [25] A.C.F. Cocks, Overview no. 117 the structure of constitutive laws for the sintering of fine grained materials, Acta Metall. Mater. 42 (1994) 2191–2210, https://doi. org/10.1016/0956-7151(94)90299-2.
- [26] J. Besson, M. Abouaf, Grain growth enhancement in alumina during hot isostatic pressing, Acta Metall. Mater. 39 (1991) 2225–2234, https://doi.org/10.1016/ 0956-7151(91)90004-K.

- [27] Y.S. Kwon, K.T. Kim, High temperature densification forming of alumina powder—constitutive model and experiments, J. Eng. Mater. Technol. 118 (1996) 448–455, https://doi.org/10.1115/1.2805941.
- [28] M.N. Rahaman, L.C. De Jonghe, G.W. Scherer, R.J. Brook, Creep and densification during sintering of glass powder compacts, J. Am. Ceram. Soc. 70 (1987) 766–774, https://doi.org/10.1111/j.1151-2916.1987.tb04877.x.
- [29] J. Besson, M. Abouaf, Rheology of porous alumina and simulation of hot isostatic pressing, J. Am. Ceram. Soc. 75 (1992) 2165–2172, https://doi.org/10.1111/ j.1151-2916.1992.tb04479.x.
- [30] M. Abouaf, J.L. Chenot, G. Raisson, P. Bauduin, Finite element simulation of hot isostatic pressing of metal powders, Int. J. Numer. Methods Eng. 25 (1988) 191–212, https://doi.org/10.1002/nme.1620250116.
- [31] E. Torresani, R.M. German, R. Huff, E.A. Olevsky, Influence of gravity on sintering of 3D-printed powder components, J. Am. Ceram. Soc. (2021), https://doi.org/ 10.1111/jace.18056.
- [32] E. Olevsky, T.T. Molla, H.L. Frandsen, R. Bjørk, V. Esposito, D.W. Ni, A. Ilyina, N. Pryds, Sintering of multilayered porous structures: Part I-constitutive models, J. Am. Ceram. Soc. 96 (2013) 2657–2665, https://doi.org/10.1111/jace.12375.
- [33] R.M. German, The Emergence of Quantitative Sintering Theory from 1945 to 1955 69 (n.d.). https://doi.org/10.1007/s11837-016-2242-1.,.
- [34] C. Van Nguyen, S.K. Sistla, S. Van Kempen, N.A. Giang, A. Bezold, C. Broeckmann, F. Lange, A comparative study of different sintering models for Al2O3, J. Ceram. Soc. Jpn. 124 (2016) 301–312, https://doi.org/10.2109/jcersj2.15257.
- [35] C.R. Alberto, E.A. Olevsky, E. Hryha, M. Persson, Modelling of δ-ferrite transformation effect on the sintering behaviour of 316L binder jetted components, in: WorldPM 2022, EPMA, Lyon, France, 2022.
- [36] Y. Wu, R.M. German, D. Blaine, B. Marx, C. Schlaefer, Effects of residual carbon content on sintering shrinkage, microstructure and mechanical properties of injection molded 17-4 PH stainless steel, J. Mater. Sci. 37 (2002) 3573–3583, https://doi.org/10.1023/A:1016532418920.
- [37] Y. Wu, D. Blaine, B. Marx, C. Schlaefer, R.M. German, Sintering densification and microstructural evolution of injection molding grade 17-4 PH stainless steel powder, Metall Mater Trans A Phys Metall Mater Sci 33 (2002) 2185–2194, https://doi.org/10.1007/s11661-002-0050-4.
- [38] A. Cabo Rios, T. Mishurova, L. Cordova, M. Persson, G. Bruno, E. Olevsky, E. Hryha, Ex-situ characterization and simulation of density fluctuations evolution during sintering of binder jetted 316L, Mater. Des. 238 (2024) 112690, https://doi. org/10.1016/j.matdes.2024.112690.
- [39] B.J. Paudel, D. Conover, J.K. Lee, A.C. To, A computational framework for modeling distortion during sintering of binder jet printed parts, J Micromech Mol Phys 6 (2021) 95–102, https://doi.org/10.1142/S242491302142008X.
- [40] K. Zhang, W. Zhang, R. Brune, E. Herderick, X. Zhang, J. Cornell, J. Forsmark, Numerical simulation and experimental measurement of pressureless sintering of stainless steel part printed by Binder Jetting Additive Manufacturing, Addit. Manuf. 47 (2021) 102330, https://doi.org/10.1016/j.addma.2021.102330.

- [41] S. Sadeghi Borujeni, A. Shad, K. Abburi Venkata, N. Günther, V. Ploshikhin, Numerical simulation of shrinkage and deformation during sintering in metal binder jetting with experimental validation, Mater. Des. 216 (2022) 110490, https://doi.org/10.1016/j.matdes.2022.110490.
- [42] J.G. Argüello, M.W. Reiterer, K.G. Ewsuk, Verification, performance, validation, and modifications to the sovs continuum constitutive model in a nonlinear large-deformation finite element code, J. Am. Ceram. Soc. 92 (2009) 1442–1449, https://doi.org/10.1111/j.1551-2916.2009.03008.x.
- [43] V.V. Skorohod, Rheological Basis of the Theory of Sintering, 1972.
- [44] E.A. Olevsky, C. Garcia-Cardona, W.L. Bradbury, C.D. Haines, D.G. Martin, D. Kapoor, Fundamental aspects of spark plasma sintering: II. Finite element analysis of scalability, J. Am. Ceram. Soc. 95 (2012) 2414–2422, https://doi.org/ 10.1111/i.1551-2916.2012.05096.x.
- [45] M.W. Reiterer, K.G. Ewsuk, J.G. Argüello, An arrhenius-type viscosity function to model sintering using the Skorohod-Olevsky viscous sintering model within a finite-element code, J. Am. Ceram. Soc. 89 (2006) 1930–1935, https://doi.org/ 10.1111/j.1551-2916.2006.01041.x.
- [46] K.K. Chawla, Micromechanics of composites, composite materials, 177–203, https://doi.org/10.1007/978-1-4757-3912-1\_10, 1987.
- [47] A. Reuss, Berechnung der Fließgrenze von Mischkristallen auf Grund der Plastizitätsbedingung für Einkristalle, ZAMM - Journal of Applied Mathematics and Mechanics/Z. Angew. Math. Mech. 9 (1929) 49–58, https://doi.org/10.1002/ ZAMM.19290090104.
- [48] Structural mechanics module user's guide, COMSOL Multiphysics® V. 6.2, COMSOL AB, Stockholm, Sweden, 2023 (n.d.).
- [49] MATLAB Version 9.13.0.2126072 (R2022b) Update 3, 2022.
- [50] K.T. Kim, Y.C. Jeon, Densification behavior and grain growth of tool steel powder under high temperature, Acta Mater. 46 (1998) 5745–5754, https://doi.org/ 10.1016/S1359-6454(98)00261-4.
- [51] S. Mirzababaei, S. Pasebani, A review on binder jet additive manufacturing of 316L stainless steel, Journal of Manufacturing and Materials Processing 3 (2019) 82, https://doi.org/10.3390/jmmp3030082.
- [52] A. Mostafaei, E.L. Stevens, E.T. Hughes, S.D. Biery, C. Hilla, M. Chmielus, Powder bed binder jet printed alloy 625: densification, microstructure and mechanical properties, Mater. Des. 108 (2016) 126–135, https://doi.org/10.1016/j. matdes.2016.06.067.
- [53] A. Pellegrini, M.G. Guerra, F. Lavecchia, Shrinkage evaluation and geometric accuracy assessment on 17–4 PH samples made by material extrusion additive manufacturing, J. Manuf. Process. 109 (2024) 394–406, https://doi.org/10.1016/ JJMAPRO.2023.12.031.
- [54] B. Barthel, S.B. Hein, C. Aumund-Kopp, F. Petzoldt, Influence of particle size distribution in metal binder jetting – effects on the properties of green and sintered parts, in: Procedia EuroPM 2019: International Powder Metallurgy Congress and Exhibition. 2019.